Chapter 6

Future Direction I: Ultrahigh-Density Two-Dimensional Nano-Hole Arrays

The contents presented in this chapter are not yet published when the thesis is written.

6.1 Introduction

In previous chapters, we have demonstrated how the Superlattice Nanowire Pattern Transfer (SNAP) method[1,2] can be used to produce highly-ordered, ultra-high density arrays of one-dimensional nanostructures, including conventional superconductor nanowires (Chapter 2),[3] high-temperature superconductor nanowires (Chapter 3),[4] one-dimensional and quasi-one-dimensional granular electronic materials (Chapter 4),[5] and one-dimensional arrays of coupled quantum dots (Chapter 5).[6] In this chapter, we discuss how SNAP can be used to produce highly-ordered, ultrahigh-density two-dimensional (2D) arrays, with a focus on nano-hole arrays. Exciting new physics is also discovered in such interesting novel structures.

The most straightforward way to produce ultrahigh-density 2D arrays using SNAP is to place an array of SNAP nanowires (NWs) on top of and perpendicular to another array of SNAP NWs. A crossbar structure[7] is thus obtained (Fig. 6-1A, upper-left), and we have recently demonstrated how such structures can be utilized to construct ultrahigh-density memory circuits.[8]

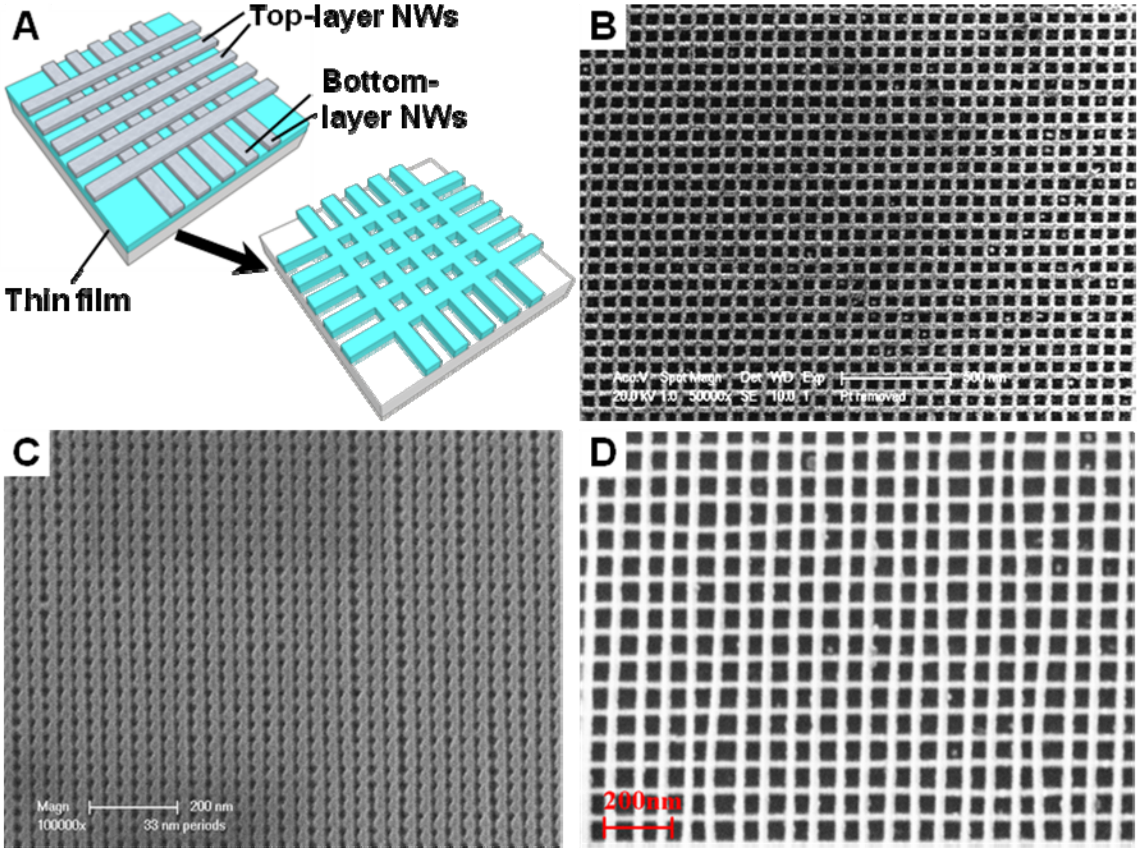

Figure 6-1. Fabrication of ultrahigh-density two-dimensional nano-hole arrays. (A): Schematic drawing of the fabrication process. (Upper-left): an array of SNAP nanowires (NWs) is placed on top of and perpendicular to another array of SNAP NWs, resulting in a crossbar structure. (Lower-right): Using the crossbar structure as a mask, high-directional dry etching produces a two-dimensional nano-hole array in the underlying thin film (cyan). (B)-(D): Scanning electron microscope images of: (B) A nano-hole array in a SiO_2 film. Pitch (spatial periodicity) =70 nm, and hole size ~50 nm. Scale bar: 500 nm. (C) A nano-hole array in a SiO_2 film. Pitch =33 nm, and hole size ~15 nm. Scale bar: 200 nm. (D) A nano-hole array in a Nb film. Pitch =70 nm, and hole size ~50 nm. Scale bar: 200 nm.

By using the crossbar structure as an etching mask for highly-directional dry etching, in this chapter we demonstrate that ultrahigh-density 2D arrays of nanometer-sized holes (nano-holes) can be produced in an underlying film of various materials (Fig. 6-1A, lower-right), basing on which new physics can be explored. Si, SiO_2, and Nb films are all found to be compatible with this fabrication method, but in principle this method should be generally applicable to any film. Scanning electron microscope (SEM) images of representative nano-hole 2D arrays thus fabricated in SiO_2 and Nb films are given in Fig. 6-1,B-D. The fabrication method itself has been demonstrated before with silicon as a proof of concept,[9] but no physical property measurements or applications of such interesting structures have been reported before.

6.2 Assembly of quantum dots into ultrahigh-density two-dimensional arrays

The fabricated nano-hole 2D arrays in SiO_2 films were first utilized in the study of templated-assisted self-assembly of quantum dots (QDs) into ultrahigh-density 2D arrays.

Previously studies on templated-assisted assembly have worked with particles with sizes range from microns to 50 nm,[10-12] and it was unclear whether the method would work for smaller particles due to the presence of Brownian motion.[10] In addition, for 2D arrays, the smallest pitch (spatial periodicity) of the array ever reported was >250 nm.[12]

In Chapter 4, we have demonstrated how SNAP nanotrenches in SiO_2 films can be utilized to assemble 5 nm and larger QDs into ordered one-dimensional and quasi-one-dimensional arrays. Similar methods are used here to assemble QDs into nano-hole 2D arrays in SiO_2 films. Nano-hole 2D arrays similar to the one presented in Fig. 6-1B are surface-functionalized with hexamethyldisilazane, and dip-coated in a toluene solution of QDs.

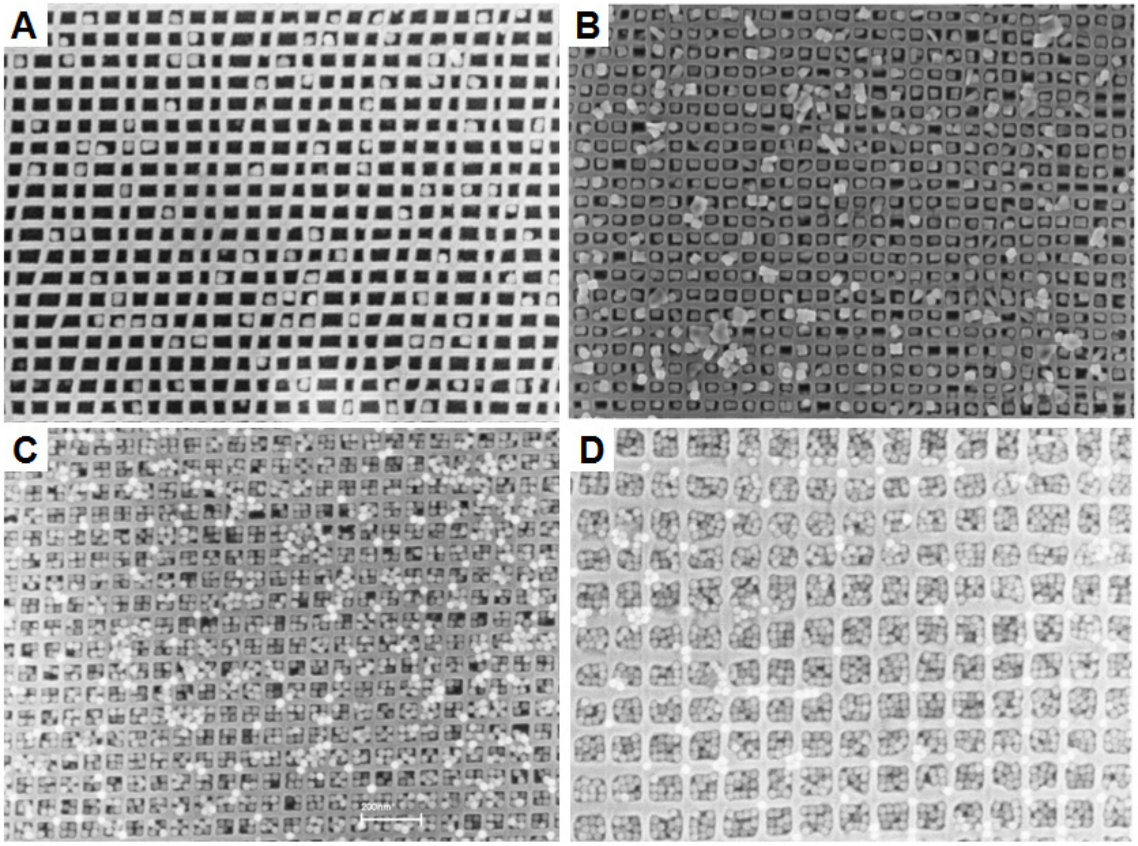

Figure 6-2. Preliminary results on assembling quantum dots (QDs) into ultrahigh-density two-dimensional arrays. Scanning electron microscope images are given for the assembly of QDs into nano-hole arrays of the same dimensions: pitch (spatial periodicity) = 70 nm, and hole size ~50 nm. (A): Assembly of ~40 nm QDs at low QD coverage. (B): Assembly of ~40 nm QDs at high QD coverage. (C): Assembly of 25 nm QDs. (D) Assembly of 15 nm QDs.

Preliminary results are shown in Fig. 6-2. Closest-packed QDs fill the nano-holes. By keeping the same dimensions for the nano-hole arrays (pitch = 70 nm, hole size ~50 nm), the packing arrangement of QDs in each nano-hole can be controlled by varying the QD size. For ~40 nm QDs, each nano-hole accommodates no more than one QD (Fig. 6-2AB), while the occupancy rate of nano-holes can be tuned by varying the QD surface coverage (Fig. 6-2AB), which in turn can be controlled by varying the concentration of the QD solution or the dip-coating speed, as discussed in Chapter 4. For 25 nm QDs, 2-by-2 square packing in each nano-hole is typically observed (Fig. 6-2C). For 15 nm QDs, ~3-by-3 packing in each nano-hole is observed (Fig. 6-2D), although disorders do exist for this particular array used in the preliminary study. Similarly, QD arrangement can also be tuned by fixing the QD size, but varying the dimensions of the nano-hole arrays.

Our results indicate that templated-assisted assembly is feasible at ~10 nm length scales. The obtained 2D arrays of QDs can serve as an interesting platform for studying new physics. Because the pitches of the arrays are very small (~50 nm), and the SNAP NWs, which serve as separating walls, are very thin, the distances between QDs in neighboring nano-holes are very small (10-20 nm) and can be adjusted precisely during SNAP fabrication. These distances are suitable for the study of surface plasmon interactions between metallic QDs, in which the packing arrangement of QDs and inter-QD distances are both important in determining the collective and local optical properties of the system.[13-16] In addition, because the conductive QDs are compartmentalized into individual nano-holes and electronically isolated from the QDs in other nano-holes (the SiO_2 substrate is insulating), the structures shown in Fig. 6-2 can sever as an ideal platform for the fabrication of QD floating gate memories[17,18] in which information is stored as charges trapped within the QDs inside each nano-hole. These studies represent future directions that need to be explored.

6.3 Superconductor films patterned with ultrahigh-density two-dimensional arrays of nano-holes

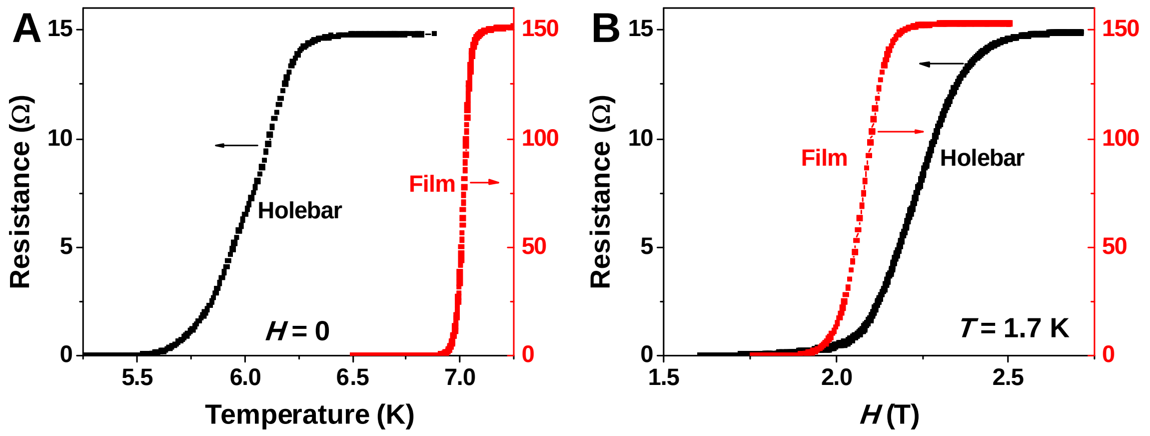

Figure 6-3. Resistance measurements on a Nb holebar and an unpatterned Nb film. For the holebar, pitch (spatial periodicity) of the nano-hole array is 33 nm, and hole size is 17 nm; width w = 6 µm and length L = 5 µm. For the film, w = 10 µm and L = 180 µm. The film thickness, h, is 11 nm for both the holebar and the unpatterned film. (A): Temperature dependence of four-point resistance at zero applied magnetic field. (B): Four-point resistance measured as a function of applied magnetic field H at base temperature (1.7 K).

The experience we gained from the fabrication of superconductor NW arrays (Chapter 2[3] and Chapter 3[4]) has recently allowed for the fabrication of superconductor films patterned with ultrahigh-density 2D arrays of nano-holes (e.g., Fig. 6-1D). The electrical properties of such patterned films are found to be significantly different from unpatterned films. For this study we are more concerned about the properties of the patterned *films* rather than the nano-holes themselves, and we shall henceforth refer to “a film patterned with ultrahigh-density 2D arrays of nano-holes" as "a holebar" for simplicity.

Fig. 6-3 presents the resistance measured on a Nb holebar with 17 nm nano-holes patterned at a pitch (spatial periodicity, or hole-to-hole distance) of p = 33 nm, patterned in a 11 nm thick film. Because our fabrication method starts from a thin film, the electrical properties of the holebar can be directly compared with those of an unpatterned film that is exactly the same as the starting film of the holebar. The superconducting critical temperature, T_c, of the holebar is reduced by ~1 K comparing to the unpatterned film (Fig. 6-3A), and the transition temperature width is broadened, suggesting impairment of superconductivity caused by the presence of nano-holes (voids). On the other hand, at base temperature the holebar is less susceptible to suppression of superconductivity from applied magnetic fields (Fig. 6-3B), and partial superconductivity can be retained at higher fields.

Also from the data presented in Fig. 6-3, the normal-state resistivity of the unpatterned film is calculated to be 9.2 μΩ cm, in agreement with previous studies on Nb films of similar thicknesses.[19,20] Assuming the same resistivity for the holebar, the effective current-carrying width (w_{eff}) of the holebar is calculated to be 2.85 μm, basing on the measured normal-state resistance and the known holebar length. w_{eff} is about half the width of the holebar (6 μm), which is plausible since half of the width of the holebar is holes. Thus for the two devices presented in Fig. 6-3, the width of the unpatterned film (10 μm) is 10/2.85 ~ 3.5 times larger than the effective width of the holebar (2.85 μm). This scaling factor turned out to be important for understanding the critical current behaviors as will be discussed below.

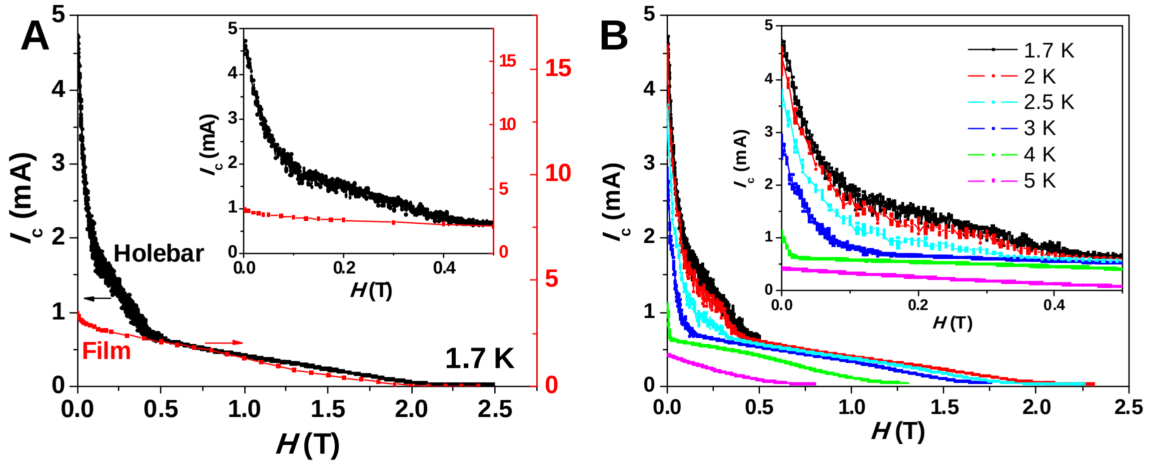

Figure 6-4. Measured critical current as a function of the applied magnetic field, H. (A): Critical current (I_c) measured at base temperature (1.7 K) for the same holebar and unpatterned film as discussed in Fig. 6-3. The critical current of the film is drawn on the scale shown on the right. Inset: expanded plot for H < 0.5 T. (B): Critical current of the holebar measured at varied temperatures. Inset: expanded plot for H < 0.5 T.

Fig. 6-4A presents the critical current (I_c) measured at base temperature (1.7 K) for the same holebar and unpatterned film as discussed in Fig. 6-3, as a function of the applied magnetic field, H. The critical current density of the unpatterned film, J_c, is 3.2×10^6 A/cm^2 at $H = 0$. This value is in agreement with the highest J_c obtained in previously studies on unpatterned Nb thin films,[21-23] as well as Nb thin films patterned with nano-holes at spatial periods of 100 nm and larger.[24] Because for thin films I_c are directly proportional to the cross section area, to compensate for the width differences between the holebar and the unpatterned film, the critical current of the unpatterned film is drawn on a scale that is 3.5 times larger than the one used for the holebar, as shown on the right axis. By doing so, one immediately notices that for H >0.5 T, the critical current behavior of the holebar is essentially the same as the unpatterned film, and I_c increases near linearly as *H* decreases. For *H* <0.5 *T*, however, I_c of the holebar suddenly starts to increase rapidly, and a ~5-fold enhancement of I_c is observed comparing to the unpatterned film at *H* = 0. This enhancement is so significant that even when the absolute value of I_c is compared, the 6 μm wide holebar still have large I_c than the 10 μm wide film. Fig. 6-4B presents the I_c-*H* relationship of the holebar measured at varied temperatures. For higher temperature, the enhancement of I_c occurs at lower *H*, and at *H* = 0 the enhancement is less than observed at base temperature. The enhancement vanishes for *T* > ~4 K. Interestingly, for all temperatures, for *H* higher than the *H* at which enhancement occurs, the measured I_c always follows the same, near linear I_c-*H* relationship similar to that of the film.

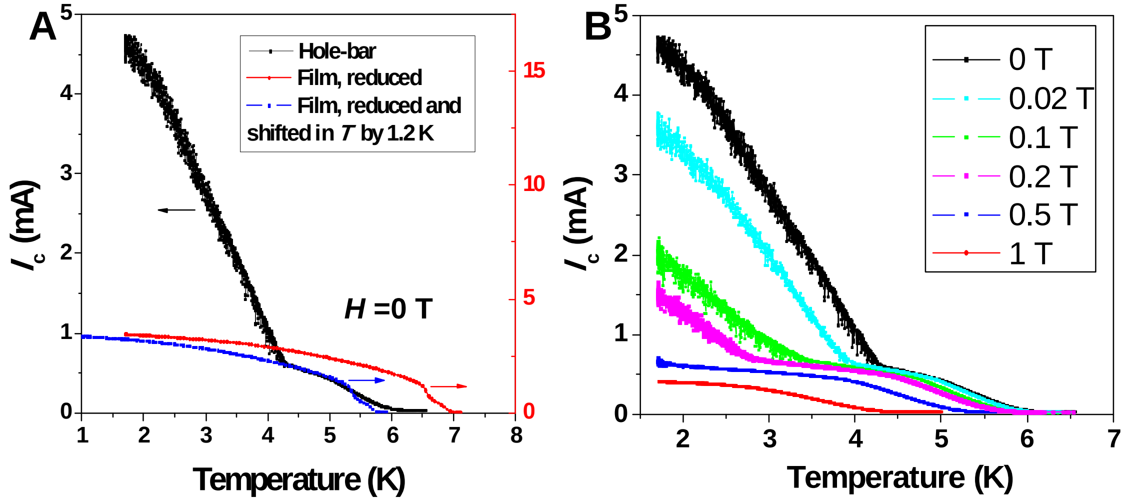

Figure 6-5. Measured critical current as a function of temperature. (A) Critical current (*I*c) measured at zero applied magnetic field for the same holebar and unpatterned film as discussed in Fig. 6-3. The critical current of the film is drawn on the scale shown on the right. The blue curve is obtained by shifting the film data to the left by 1.2 K, to compensate for the lower *T*c of the holebar. (B) Critical current of the holebar measured at varied magnetic fields, *H*.

Fig. 6-5 presents the I_c measured as a function of temperature. Fig. 6-5A compares the I_c behavior of the holebar to the unpatterned film, measured at zero applied magnetic field. After rescaling the I_c of the film by 3.5 times, and shifting the curve by 1.2 K to compensate for the lower T_c observed in the holebar, the I_c behavior of the holebar is found to be the same as the unpatterned film for $T > 4.2$ K. For $T < 4.2$ K, however, enhancement of I_c is again observed in the holebar. The enhancement is very sensitive to the applied magnetic field, and decreases rapidly at higher H (Fig. 6-5B). The enhancement vanishes at ~0.5 T for the base temperature of 1.7 K. These observations are in agreement with the results in Fig. 6-4. Again, very interestingly, for all H, for temperatures higher than the temperature at which the enhancement occurs, the measured I_c in holebar always follows the same I_c-H relationship similar to that of the unpatterned film.

The above results suggest I_c can be drastically enhanced in holebars at low H and low T, whereas at high H and high T, nano-hole arrays have no effects on I_c, and the holebar behaves like a continuously film, except for the slight decrease in T_c. It's also instructive to note that a significant increase in the noise/uncertainty of I_c always accompanies the I_c enhancement (Fig. 6-4 and Fig. 6-5). This is indicative of the presence of dynamic effects in the system.

The appearance of resistance (and therefore, the loss of superconductivity) in an unpatterned superconductor thin film at I_c is often caused by the motion of supercurrent vortices.[25] Magnetic fields penetrate the superconductor film through normal cores that appear evenly over the entire film. Each normal core has a diameter of the temperature-dependent superconducting coherence length $\xi(T)$ [for Nb, $\xi(0)$ ~40 nm], and is surrounded by a vortex of supercurrent. The magnetic flux through each normal core is a fixed flux quantum, $\Phi_0 = hc/2e = 2.07 \times 10^{-7}$ G·cm^2. In the presence of a transport current, the core-vortex bundles experience a Lorentz force tending to make them move at a right angle to the current direction, in which case a longitudinal, “resistive” voltage would be induced. At low current levels, however, the core-vortex bundles can be pinned down at local defects within the superconductor, and so there is no motion of the vortices and no resistive voltage is registered, i.e., the film still appears superconducting. Holes artificially patterned in a superconductor film can serve as local defects and thus pinning centers for vortices, and so may enhance J_c of the film.

Previous studies on superconductor thin films patterned with hole arrays have focused on the case in which the pitch of holes (hole-to-hole distance) in the array, p, is larger than 100 nm and therefore $>> \xi(0)$.[24,26-33] Because $\xi(T) \approx \xi(0)(1-T/T_c)^{-1/2}$, for $T \sim T_c$, $\xi(T)$ is large and can be comparable to the pitch of holes. Therefore, for $T \sim T_c$ the holes in such systems can effectively serve as pinning centers for supercurrent vortices, the cores of which have a size of $\sim\xi(T)$. Enhancement of J_c has thus been reported. For $T << T_c$, however, interstitial vortices appear within the superconductor, and the enhancement of J_c vanishes. In addition, by pinning down vortices at local holes, J_c is typically only significant enhanced for finite applied magnetic fields, while for $H = 0$, the measured J_c are similar to unpatterned films.[24,34] Similar results were also observed in nanorod/superconductor composites in which nanorods act as pinning columnar defects: enhancement of J_c is more pronounced at high T and high H.[35,36]

Our system is in the opposite limit, $p <\sim \xi(0)$, and so reflects completely different physics. For $T << T_c$, $\xi(T) \sim \xi(0) \sim p$, so supercurrent vortices can form (and are pinned down) around individual nanoholes, and significantly enhanced J_c is observed. Interstitial vortices cannot form within the superconductor at any temperature, since the width of superconductor wires in the holebar are ~$p/2 \sim \xi(0)/2$. On the other hand, for $T \sim T_c$, $\xi(T) >> p$. In this regime, the local voids are too small and too close to each other for the superconducting electrons to "see", and so the holebar behaves like a continuous film, although with reduced T_c. Similarly, an applied magnetic field also leads to increased $\xi(T)$, and so the holebar also behaves like a film at high H. The observed clear transition between holebar and film behaviors at certain T and H has not been reported before according to our knowledge. Future experiments on holebars of different dimensions are necessary to further elucidate the mechanisms that lead to the observed J_c behavior.

6.4 References

[1] N. A. Melosh, A. Boukai, F. Diana, B. Gerardot, A. Badolato, P. M. Petroff, and J. R. Heath, "Ultrahigh-density nanowire lattices and circuits," *Science,* **300**, 112-115 (2003).

[2] J. R. Heath, "Superlattice Nanowire Pattern Transfer (SNAP)," *Accounts of Chemical Research,* **41**, 1609-1617 (2008).

[3] K. Xu and J. R. Heath, "Controlled fabrication and electrical properties of long quasi-one-dimensional superconducting nanowire arrays," *Nano Letters,* **8**, 136-141 (2008).

[4] K. Xu and J. R. Heath, "Long, Highly-Ordered High-Temperature Superconductor Nanowire Arrays," *Nano Letters,* **8**, 3845-3849 (2008).

[5] K. Xu, L. Qin, and J. R. Heath, "The crossover from two dimensions to one dimension in granular electronic materials," *Nature Nanotechnology,* **Advanced online publication**, 10.1038/nnano.2009.81 (2009).

[6] K. Xu, J. E. Green, J. R. Heath, F. Remacle, and R. D. Levine, "The emergence of a coupled quantum dot array in a doped silicon nanowire gated by ultrahigh density top gate electrodes," *Journal of Physical Chemistry C,* **111**, 17852-17860 (2007).

[7] J. R. Heath, P. J. Kuekes, G. S. Snider, and R. S. Williams, "A defect-tolerant computer architecture: Opportunities for nanotechnology," *Science,* **280**, 1716-1721 (1998).

[8] J. E. Green, J. W. Choi, A. Boukai, Y. Bunimovich, E. Johnston-Halperin, E. DeIonno, Y. Luo, B. A. Sheriff, K. Xu, Y. S. Shin, H. R. Tseng, J. F. Stoddart, and J. R. Heath, "A 160-kilobit molecular electronic memory patterned at 10^{11} bits per square centimetre," *Nature,* **445**, 414-417 (2007).

[9] D. W. Wang, Y. Bunimovich, A. Boukai, and J. R. Heath, "Two-dimensional single-crystal nanowire arrays," *Small,* **3**, 2043-2047 (2007).

[10] G. W. Crabtree, U. Welp, Z. L. Xiao, J. S. Jiang, V. K. Vlasko-Vlasov, S. D. Bader, J. Liang, H. Chik, and J. M. Xu, "Vortices in dense self-assembled hole arrays," *Physica C-Superconductivity and Its Applications,* **387**, 49-56 (2003).

[11] Y. Cui, M. T. Bjork, J. A. Liddle, C. Sonnichsen, B. Boussert, and A. P. Alivisatos, "Integration of colloidal nanocrystals into lithographically patterned devices," *Nano Letters,* **4**, 1093-1098 (2004).

[12] T. Kraus, L. Malaquin, H. Schmid, W. Riess, N. D. Spencer, and H. Wolf, "Nanoparticle printing with single-particle resolution," *Nature Nanotechnology,* **2**, 570-576 (2007).

[13] S. K. Ghosh and T. Pal, "Interparticle coupling effect on the surface plasmon resonance of gold nanoparticles: From theory to applications," *Chemical Reviews,* **107**, 4797-4862 (2007).

[14] L. M. Liz-Marzan, "Tailoring surface plasmons through the morphology and assembly of metal nanoparticles," *Langmuir,* **22**, 32-41 (2006).

[15] S. A. Maier, M. L. Brongersma, P. G. Kik, S. Meltzer, A. A. G. Requicha, and H. A. Atwater, "Plasmonics - A route to nanoscale optical devices," *Advanced Materials,* **13**, 1501-1505 (2001).

[16] S. A. Maier, P. G. Kik, H. A. Atwater, S. Meltzer, E. Harel, B. E. Koel, and A. A. G. Requicha, "Local detection of electromagnetic energy transport below the diffraction limit in metal nanoparticle plasmon waveguides," *Nature Materials,* **2**, 229-232 (2003).

[17] M. L. Ostraat, J. W. De Blauwe, M. L. Green, L. D. Bell, M. L. Brongersma, J. Casperson, R. C. Flagan, and H. A. Atwater, "Synthesis and characterization of aerosol silicon nanocrystal nonvolatile floating-gate memory devices," *Applied Physics Letters,* **79**, 433-435 (2001).

[18] P. Punchaipetch, Y. Uraoka, T. Fuyuki, A. Tomyo, E. Takahashi, T. Hayashi, A. Sano, and S. Horii, "Enhancing memory efficiency of Si nanocrystal floating gate memories with high-kappa gate oxides," *Applied Physics Letters,* **89**, 093502 (2006).

[19] A. I. Gubin, K. S. Il'in, S. A. Vitusevich, M. Siegel, and N. Klein, "Dependence of magnetic penetration depth on the thickness of superconducting Nb thin films," *Physical Review B,* **72**, 064503 (2005).

[20] K. Yoshii, H. Yamamoto, K. Saiki, and A. Koma, "Superconductivity and electrical-properties in single-crystalline ultrathin Nb films grown by molecular-beam epitaxy," *Physical Review B,* **52**, 13570-13575 (1995).

[21] C. A. Neugebauer and R. A. Ekvall, "Vapor-deposited superconductive films of Nb, Ta, and V," *Journal of Applied Physics,* **35**, 547-553 (1964).

[22] R. P. Huebener, R. T. Kampwirth, R. L. Martin, T. W. Barbee, and R. B. Zubeck, "Critical current density in superconducting niobium films," *IEEE Transactions on Magnetics,* **MA11**, 344-346 (1975).

[23] S. L. Prischepa, D. Montemurro, C. Cirillo, C. Attanasio, M. Salvato, V. Merlo, A. N. Lykov, and A. Y. Tsvetkov, "Thickness dependence of pinning mechanisms in granular Nb thin films," *Superconductor Science & Technology,* **19**, 1124-1129 (2006).

[24] U. Welp, Z. L. Xiao, J. S. Jiang, V. K. Vlasko-Vlasov, S. D. Bader, G. W. Crabtree, J. Liang, H. Chik, and J. M. Xu, "Superconducting transition and vortex pinning in Nb films patterned with nanoscale hole arrays," *Physical Review B,* **66**, 212507 (2002).

[25] M. Tinkham, *Introduction to Superconductivity*, 2nd ed. New York: McGraw-Hill, 1996.

[26] A. T. Fiory, A. F. Hebard, and S. Somekh, "Critical currents associated with interaction of commensurate flux-line sublattices in a perforated Al film," *Applied Physics Letters,* **32**, 73-75 (1978).

[27] M. Baert, V. V. Metlushko, R. Jonckheere, V. V. Moshchalkov, and Y. Bruynseraede, "Composite flux-line lattices stabilized in superconducting films by a regular array of artificial defects," *Physical Review Letters,* **74**, 3269-3272 (1995).

[28] K. Harada, O. Kamimura, H. Kasai, T. Matsuda, A. Tonomura, and V. V. Moshchalkov, "Direct observation of vortex dynamics in superconducting films with regular arrays of defects," *Science,* **274**, 1167-1170 (1996).

[29] X. S. Ling, H. J. Lezec, M. J. Higgins, J. S. Tsai, J. Fujita, H. Numata, Y. Nakamura, Y. Ochiai, C. Tang, P. M. Chaikin, and S. Bhattacharya, "Nature of phase transitions of superconducting wire networks in a magnetic field," *Physical Review Letters,* **76**, 2989-2992 (1996).

[30] V. Metlushko, U. Welp, G. W. Crabtree, R. Osgood, S. D. Bader, L. E. DeLong, Z. Zhang, S. R. J. Brueck, B. Ilic, K. Chung, and P. J. Hesketh, "Interstitial flux phases in a superconducting niobium film with a square lattice of artificial pinning centers," *Physical Review B,* **60**, R12585-R12588 (1999).

[31] M. I. Montero, J. J. Akerman, A. Varilci, and I. K. Schuller, "Flux pinning by regular nanostructures in Nb thin films: Magnetic vs. structural effects," *Europhysics Letters,* **63**, 118-124 (2003).

[32] M. D. Stewart, A. Yin, J. M. Xu, and J. M. Valles, "Superconducting pair correlations in an amorphous insulating nanohoneycomb film," *Science,* **318**, 1273-1275 (2007).

[33] A. Castellanos, R. Wordenweber, G. Ockenfuss, A. VonderHart, and K. Keck, "Preparation of regular arrays of antidots in $YBa_2Cu_3O_7$ thin films and observation of vortex lattice matching effects," *Applied Physics Letters,* **71**, 962-964 (1997).

[34] A. F. Hebard, A. T. Fiory, and S. Somekh, "Critical currents in Al films with a triangular lattice of 1 μm holes," *IEEE Transactions on Magnetics,* **13**, 589-592 (1977).

[35] P. D. Yang and C. M. Lieber, "Nanorod-superconductor composites: A pathway to materials with high critical current densities," *Science,* **273**, 1836-1840 (1996).

[36] P. D. Yang and C. M. Lieber, "Nanostructured high-temperature superconductors: Creation of strong-pinning columnar defects in nanorod/superconductor composites," *Journal of Materials Research,* **12**, 2981-2996 (1997).

Chapter 7

Future Direction II: Graphene Nano-Ribbon Arrays and Scanning Tunneling Microscopy

The contents presented in this chapter are not yet published when the thesis is written. The scanning tunneling microscopy part of the study is in collaboration with Peigen Cao. The graphene fabrication part is in collaboration with Wan Li (Cornell).

7.1 Introduction

Graphene is the name given to a flat monolayer of carbon atoms tightly packed into a two-dimensional (2D) honeycomb lattice.[1] As a newly discovered material,[1,2] graphene has attracted widespread research interests for its outstanding electrical and mechanical properties.[1,3]

This chapter briefly describes my ongoing research on graphene, including studies towards the fabrication of graphene nano-ribbon arrays for potential applications in nanoelectronic circuits, and scanning tunneling microscopy (STM) studies of graphene sheets on SiO_2 substrates.

7.2 Fabrication of graphene sheets

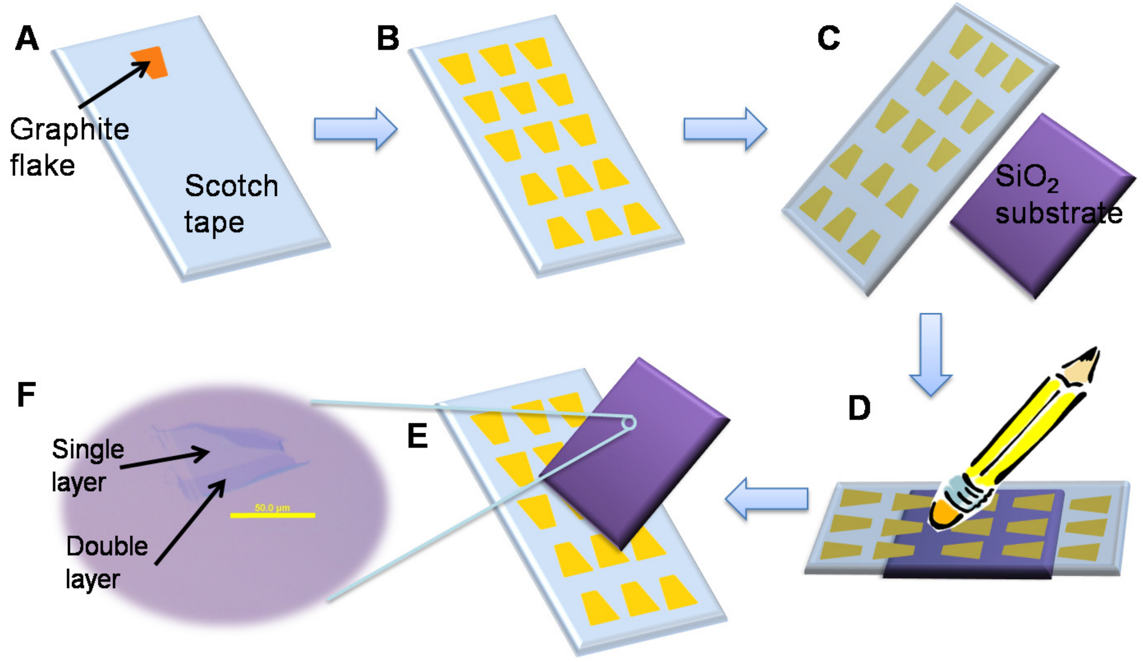

Figure 7-1. Process flow schematics for the fabrication of graphene sheets. (A): A thin graphite flake is stuck onto a scotch tape. (B): By folding and peeling the tape for ~10 times, the graphite flake is exfoliated into multiple thinner flakes, covering the entire tape surface. (C): The scotch tape is turned over, and the graphite flakes on the surface are brought into contact with a SiO_2 substrate. (D): An eraser is used to rub the back of the tape, to ensure close contact between the graphite flakes and the substrate. (E): The scotch tape is peeled off from the substrate, leaving graphene sheets and other thin graphitic layers on the SiO_2 substrate. (F): Graphene sheets on the surface are identified though an optical microscope. Single-layer and double-layer parts of the graphene sheet are labeled in graph. Scale bar: 50 µm.

The graphene sheets studied in this chapter were fabricated through mechanical exfoliation of graphite flakes, following previous studies by others.[4-6] The detailed fabrication processes are described in Fig. 7-1 and caption. The fabrication method is low-yielding, and the locations of the resultant graphene sheets are uncontrolled. After multiple trials, we were able to obtain graphene sheets ~10 μm and larger in size (Fig. 7-1F and Fig. 7-2A).

Remarkably, although only one atomic-layer thick, graphene sheets are visible in an optical microscope when placed on top of a Si wafer with a carefully chosen thickness (300 nm or 90 nm) of SiO_2 (Fig. 7-1F and Fig. 7-2A). This is due to a feeble interference-like contrast caused by the graphene sheet with respect to an empty wafer.[1] In addition, significant color differences are observed for graphitic sheets of different number of graphene layers (Fig. 7-1F and Fig. 7-2A). The number of layers at different locations was unambiguously identified through spatially resolved Raman spectroscopy,[7,8] as shown in Fig. 7-2BC.

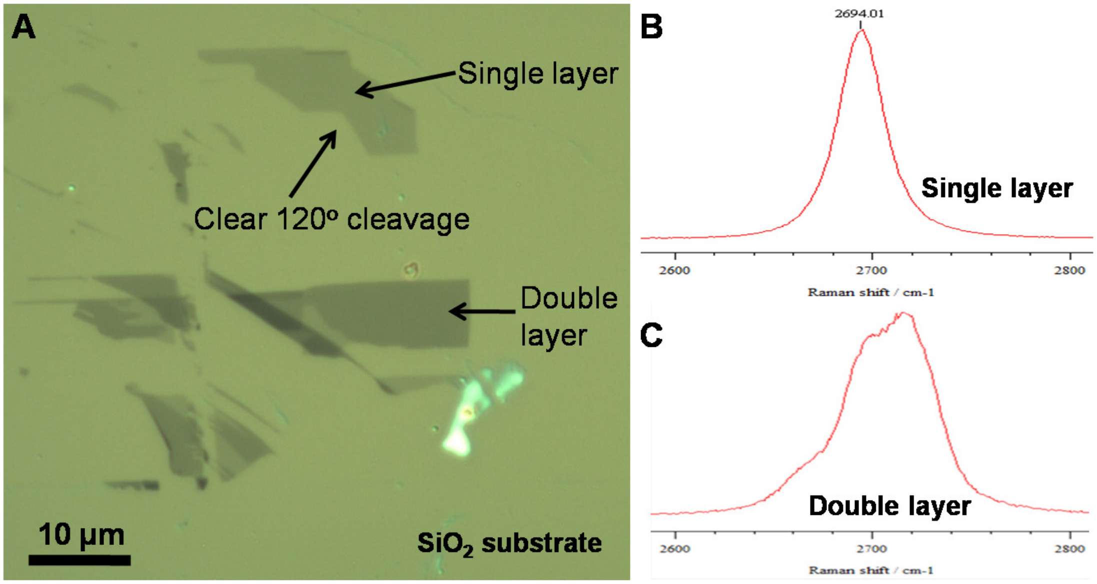

Figure 7-2. Fabricated graphene sheets on a SiO_2 substrate. (A): Optical microscope image of the fabricated graphene sheets. The number of graphene layers for different parts of the sheets were identified though Raman spectroscopy. (B): Recorded Raman spectroscopy of a single-layer graphene sheet. (C): Recorded Raman spectroscopy for a graphene double layer.

7.3 Electrical characterization and studies towards the fabrication of graphene nano-ribbon arrays

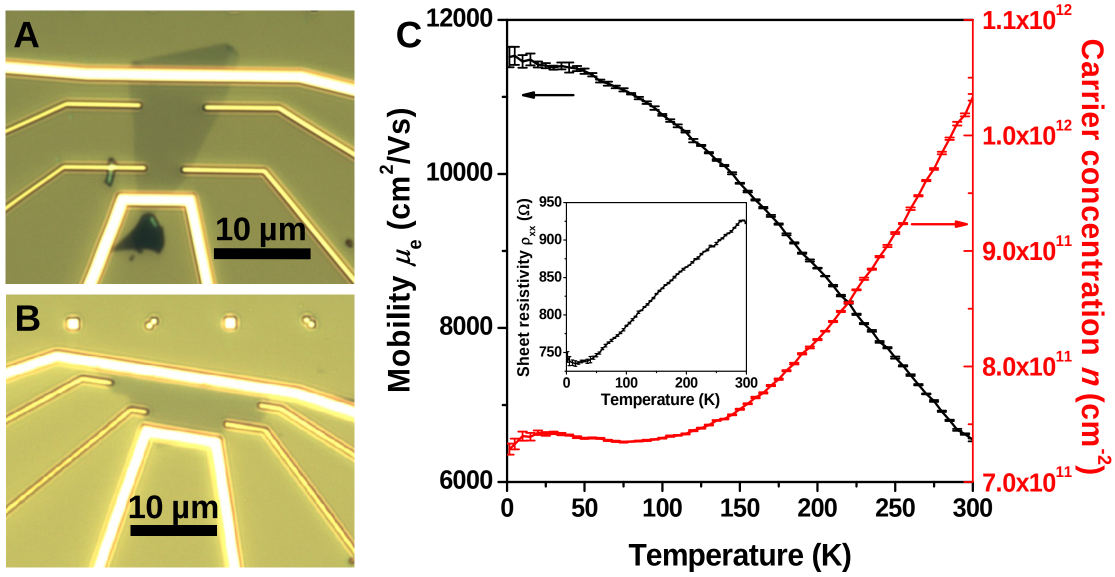

Figure 7-3. Hall effect measurements of the fabricated graphene sheets. (A) and (B): Optical microscope images of two devices for Hall measurement of graphene sheets. (C): Carrier mobility and carrier concentration of a graphene sheet measured through Hall effect, as a function of temperature. Inset: measured sheet resistivity, as a function of temperature.

The electrical properties of the fabricated graphene sheets were studied through Hall effect measurements (Fig. 7-3). Extremely high carrier mobility is found for the graphene sheets fabricated through the processes discussed above. For the *n*-type device shown in Fig. 7-3C, an electron mobility of 6,500 cm^2/Vs is measured at room temperature, which is more than 10 times higher than the typical mobility in silicon-based electronic devices. The mobility increases steadily for lower temperatures, as carrier concentration slowly decreases. For temperatures below ~50 K, The mobility reaches 11,500 cm^2/Vs.

The measured very high mobility is in agreement with previous studies,[1,2] and indicates that we have successfully fabricated high-quality graphene sheets. Because for electronic devices, higher mobility translates into higher operating speeds and other advantages, graphene is considered as a tantalizing martial for electronic applications.[1] On the other hand, graphene is a semimetal with a zero band gap, and thus very low on-off ratios are achieved in graphene-base field-effect transistors (FETs) at room temperature. One way to open up the band gap for room temperature FET operation is to pattern graphene sheets into ~10 nm wide ribbons (nano-ribbons).[9-12]

As discussed in previous chapters, the Superlattice Nanowire Pattern Transfer (SNAP) method[13,14] provides a unique way to fabricate highly-ordered, ultrahigh-density arrays of one-dimensional nanostructures out of various films. The major challenge to implement SNAP and fabricate ultrahigh-density arrays of nano-ribbons from a graphene sheet is that graphene is unstable in aqua regia, the use of which is necessary to remove Pt nanowires that serve as etch masks for the nanowire pattern translation.[13] One possible way to solve this problem is to protect the graphene surface with a thin layer of SiO_2 before Pt nanowires are deposited, so the Pt nanowires can be later removed with physical dry etching, similar to the fabrication processes for superconductor nanowires (Chapter 3). The presence of a SiO_2 protect layer, however, is undesirable for FET devices, and complicates the implementation of top gate structures.

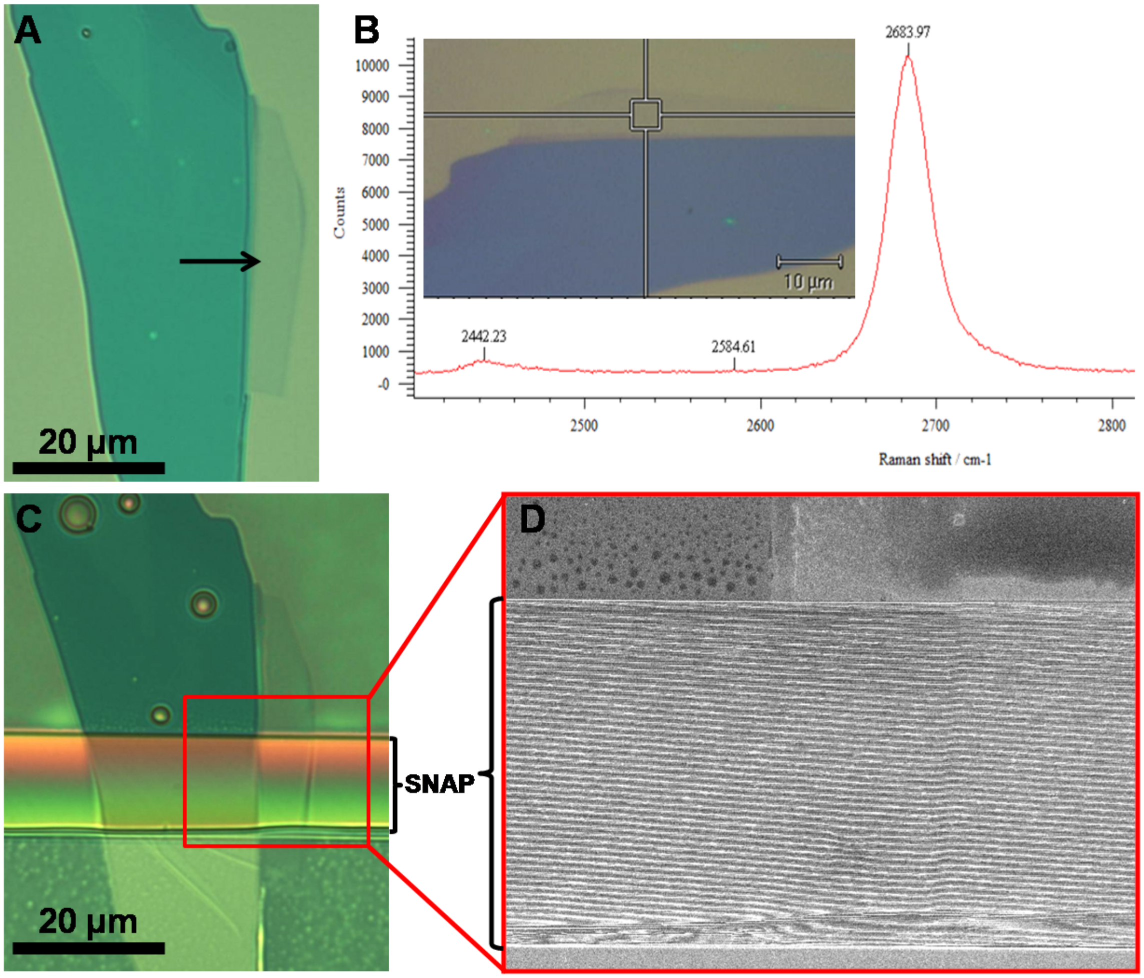

Figure 7-4. A NiCr SNAP nanowire array on graphene. (A): An optical microscope image of a pristine single-layer graphene sheet (pointed to by the arrow), next to a ~10 layer-thick graphitic sheet (on the left). (B): Recorded local Raman spectroscopy of the graphene sheet in (A). Inset: An optical image showing the location where the local Raman spectroscopy was performed (within the square at the crosshairs). (C): An optical microscope image showing a NiCr SNAP nanowire array deposited on the graphene sheet. (D): A scanning electron microscope image of the region encircled by the red box in (C). The nanowires in the array are not individually resolvable at this magnification.

Alternatively, we have recently worked out the recipe to fabricate NiCr SNAP nanowires. Such NiCr NWs can be removed with the commercial etchant NiCr-TFN [$(NH_4)_2Ce(NO_3)_6$ + 5% HNO_3 + H_2O], which is found to be compatible with graphene. Fig. 7-4 presents our preliminary results on the deposition of an array of NiCr SNAP nanowires on top of a pristine single-layer graphene sheet. The array is comprised of 400 nanowires each ~17 nm in width, with a pitch (spatial periodicity) of 33 nm. Using these NiCr SNAP nanowires as an etch mask, follow-up studies will translate the SNAP nanowire patterns into the graphene sheet with an oxygen plasma. The NiCr nanowires will then be removed with NiCr-TFN, leaving behind an ultrahigh-density array of highly-ordered graphene nano-ribbons, with clean surface. The electrical properties of the graphene nano-ribbon arrays will be systematically studied, and by varying the width of the NiCr SNAP mask nanowires, the width and therefore the band gap of the resultant nano-ribbons can be controlled.

7.4 Scanning tunneling microscopy studies of graphene sheets on SiO_2 substrates

Contrary to the general assumption that graphene is a uniform, “flat” monolayer of carbon atoms, recent studies have suggested the existence of local variations in both the morphology and the electrical properties within the same graphene sheet.[15,16] In addition, in most cases graphene sheets sit on substrates (typically SiO_2 substrates, as discussed previously), and interactions between the graphene and the substrate are expected to result in additional local structural/electrical property variations. STM provides a unique way to study such local variations from the atomic scale to micrometer scales.

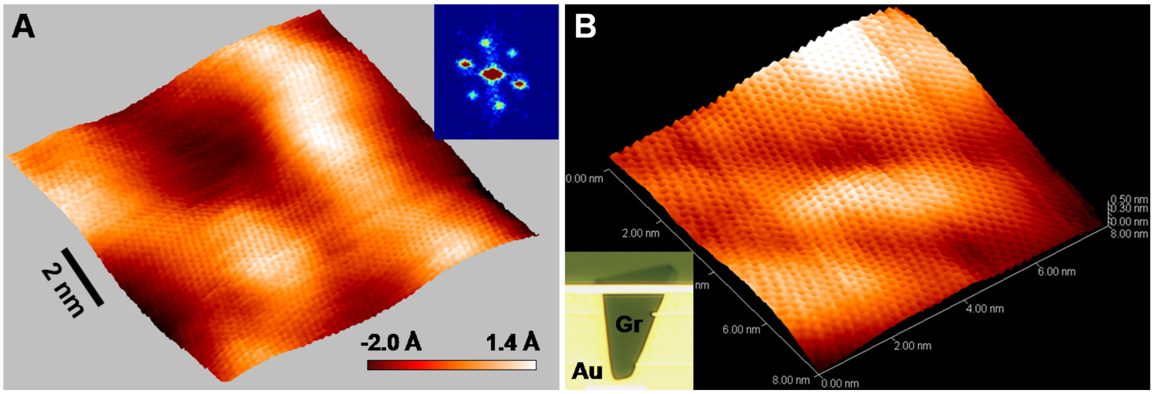

Figure 7-5. Two constant-current STM topographs of graphene sheets on SiO_2 substrates, obtained at 77 K. (A) inset: two-dimensional Fourier transform of the topograph. (B) inset: Optical microscope images of the device: the graphene sheet (Gr) is contacted at all edges by Au, so the tunneling current diffuses in-plane.

As shown in Fig. 7-5, we have achieved single-atomic resolution in our STM topographs of graphene sheets. On the Å-scale, we observed clear honeycomb structures (Fig. 7-5), with bond lengths in agreement with the known graphene lattice constant (Fig. 7-6A). On the nanometer-scale, however, we found that the graphene is not really “flat”, but instead have local height variations of ~3 Å. This is likely because the graphene sheet partially follows the underlying SiO_2 substrate,[17] which has local height variations of ~1 nm.

STM topographs obtained on graphene (Fig. 7-5 and Fig. 7-6A) are found to be fundamentally different from those obtained on bulk graphite samples (Fig. 7-6B). This is because[18,19] in graphitic films with more than one graphene layers, adjacent layers are shifted by a half crystal period with respect to each other. As a result, two different types of atoms exist in the topmost layer. One type of the atoms sits on top of an underlying atom in the underlying layer, while the other type of atoms sits on top of a hollow site.

The local electronic density is different for these two types of atoms, and in STM only one type of the atoms is observed, resulting in the "3-for-6" pattern seen in Fig. 7-6B. In contrast, without the interactions from an underlying layer, single layers of graphene always lead to STM topographs with honeycomb structures.

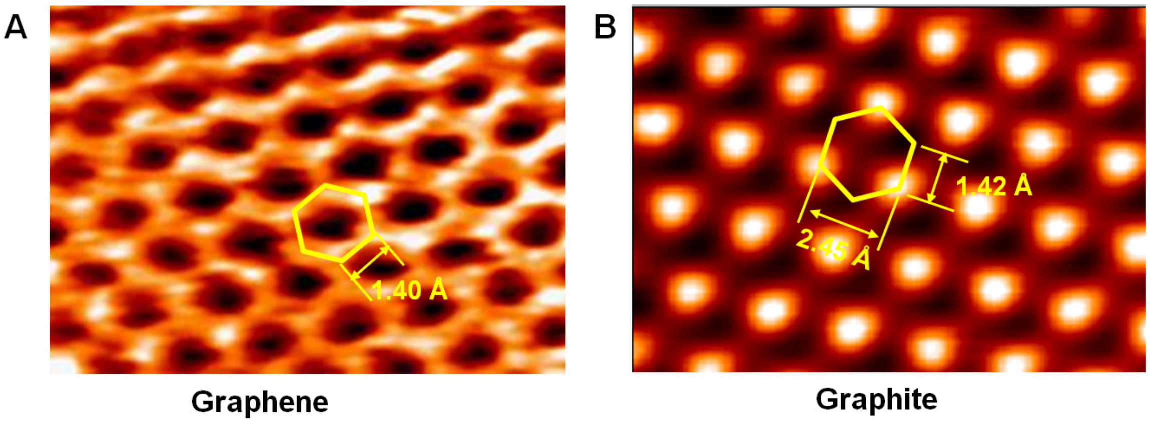

Graphene **Graphite**

Figure 7-6. STM topographs of a graphene sheet and a bulk graphite sample. (A): Order honeycomb structures are observed for a graphene sheet on a SiO_2 substrate. (B): For a bulk graphite sample, only three of the six carbon atoms in each hexagonal ring are observed.

In our study we frequently encounter "wrinkles" in graphene that are ~10 nm in width and ~2 nm in height (Fig. 7-7AB). Such structures cannot be identified through optical microscopes, and have not been reported before according to our knowledge. We found such structures to be ubiquitous in graphene sheets, and have different structures comparing to the "flat" parts of graphene. Fig. 7-7CD presents atomically-resolved topographs obtained on a wrinkle in the same graphene sheet as Fig. 7-6A. Interestingly, a "3-for-6" pattern is seen over the entire graphene wrinkle (Fig. 7-7CD), while the topograph taken on the *same* graphene sheet right next to the wrinkle keeps the honeycomb structures that are characteristic of “flat” graphene sheets.

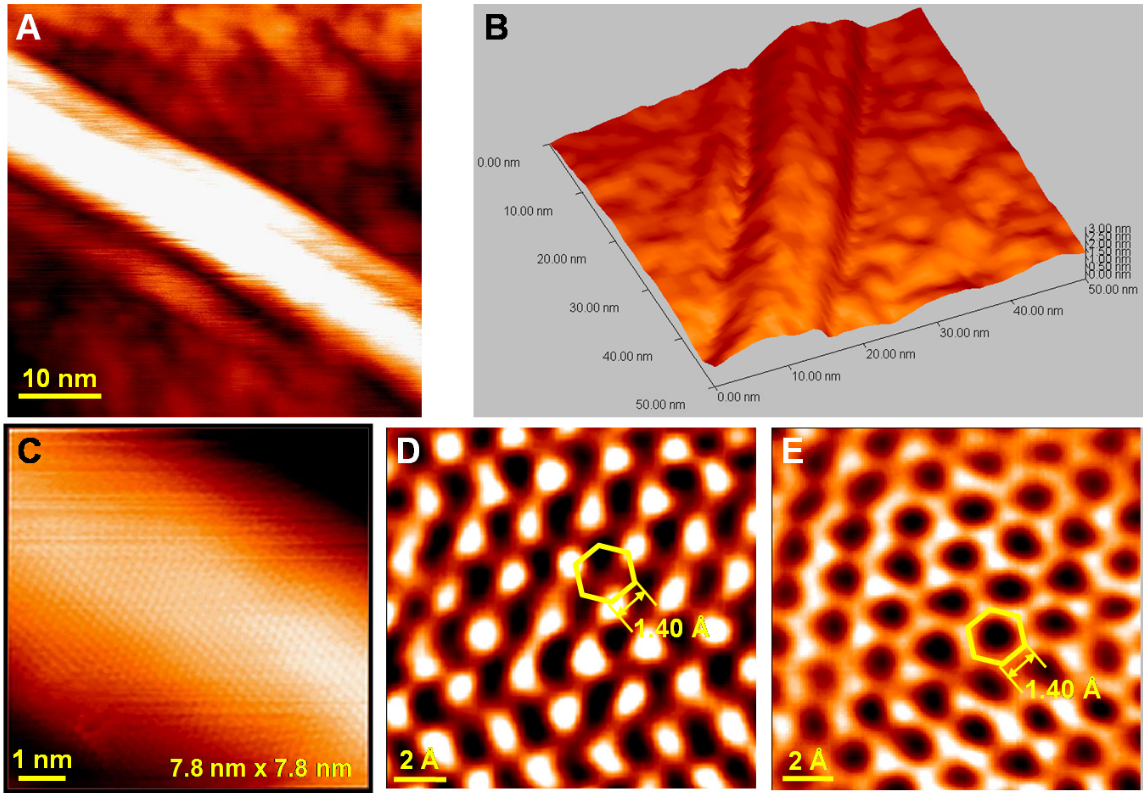

Figure 7-7. STM topographs of a graphene wrinkle. (A): A large-area scan of the graphene wrinkle. (B): A three-dimensional plot of the data in (A). Note the scale for *z*-direction is different from the scale for *x* and *y* directions. (C): The wrinkle region at a higher magnification. (D): Atomically-resolved topograph obtained on the wrinkle. (E): Atomically-resolved topograph taken on the *same* graphene sheet right next to the wrinkle, but on the “flat” surface.

Small (<1 nm) and random regions of “3-for-6” patterns have been reported before in a graphene sheet on SiO_2 substrate, and the origin of such patterns were thought to be due to either film curvature or the charge traps on the SiO_2 surface.[17] Our results suggest film curvature should be the reason for the observed “3-for-6” patterns in graphene: on the Å scale, local bending/strain in the wrinkle may break the symmetry and degeneracy of the electronic states in graphene, similar to those found in carbon nanotubes.[20] In addition, recent studies have also suggested that local bending/curvature in graphene may induce a sp^2-to-sp^3 crossover of carbon-carbon bonds, and facilitate the breaking of delocalized π-bonds in graphene.[21] In the latter case, the carbon atoms may adopt a structure similar to the chair conformation of cyclohexane, and so three of the six carbon atoms in the hexagonal ring are higher than the other three.

To understand the local variations of electrical properties, we have also utilized STM to map out the local conductance in a graphene sheet. In a previous study, a scanning single-electron transistor was used to map out the local carrier density variations in a film, but the spatial resolution of this method was lower than ~100 nm.[16] STM should uniquely enable the mapping of local conductance variations in graphene from the atomic scale to micrometer scales, but such study has not been reported before.

Fig. 7-8 presents our preliminary data on STM mapping of local conductance at low (~10 mV) biases. Fig. 7-8AB indicate that the wrinkle has significantly lower conductance comparing to other parts of graphene. This is in agreement with our previous discussions that the local electronic states are affected by the bending/curvature effects. In particular, significantly reduced conductance can be expected if delocalized π-bonds are indeed broken. Fig. 7-8CD further indicate that higher conductance is often seen at the locations where the graphene is in touch with the edges of the underlying SiO_2 substrate. This suggests local conductance enhancement as a result of phonon-coupling from the SiO_2 substrate.

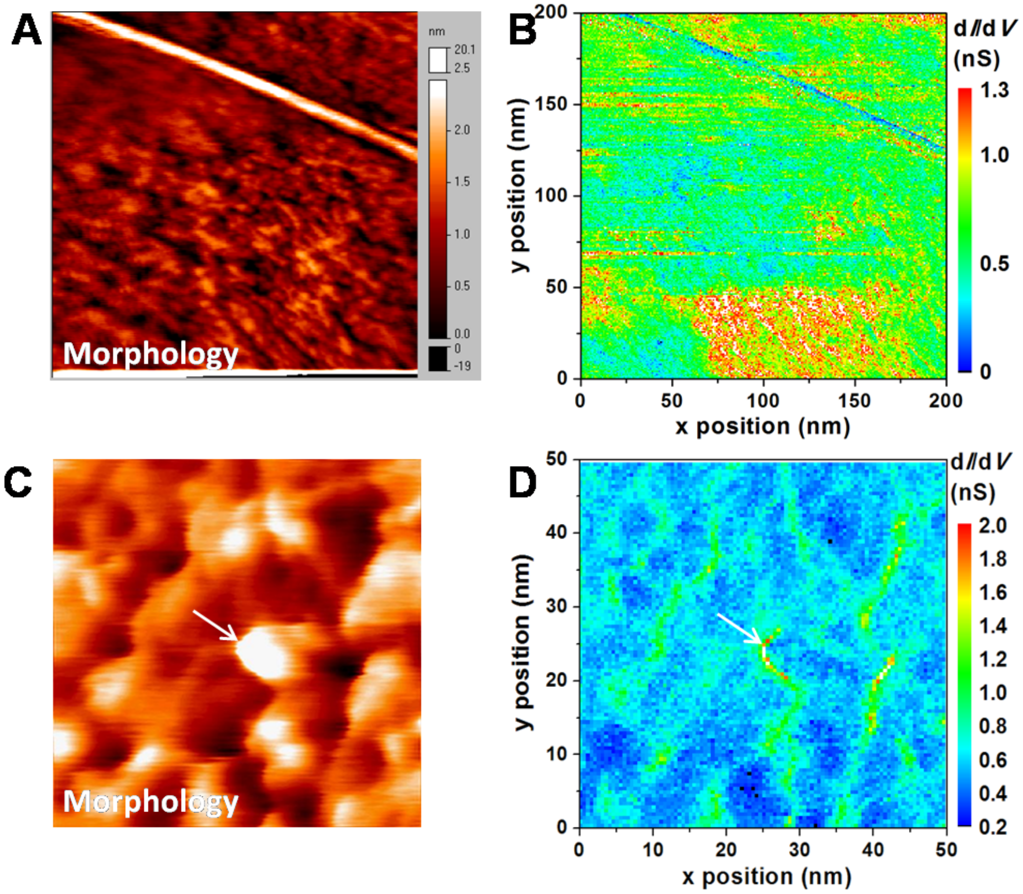

Figure 7-8. STM mapping of local conductance variations. (A): An STM topograph of a graphene sheet on a SiO_2 substrate. A wrinkle is seen in the upper part of the graph. (B): A map of local conductance measured over the same region shown in (A). (C): An STM topograph of a graphene sheet on a SiO_2 substrate. White arrow points to where the graphene is believed to be in touch with the edges of the underlying SiO_2 substrate. (D): A map of local conductance measured over the same region shown in (C).

Our STM results suggest large local variations in both the morphology and the electrical properties of the same graphene sheet, challenging previous assumptions. These results have important implications for future studies.

7.5 References

[1] A. K. Geim and K. S. Novoselov, "The rise of graphene," *Nature Materials,* **6**, 183-191 (2007).

[2] K. S. Novoselov, A. K. Geim, S. V. Morozov, D. Jiang, Y. Zhang, S. V. Dubonos, I. V. Grigorieva, and A. A. Firsov, "Electric field effect in atomically thin carbon films," *Science,* **306**, 666-669 (2004).

[3] A. H. C. Neto, F. Guinea, N. M. R. Peres, K. S. Novoselov, and A. K. Geim, "The electronic properties of graphene," *Reviews of Modern Physics,* **81**, 109-162 (2009).

[4] K. S. Novoselov, D. Jiang, F. Schedin, T. J. Booth, V. V. Khotkevich, S. V. Morozov, and A. K. Geim, "Two-dimensional atomic crystals," *Proceedings of the National Academy of Sciences of the United States of America,* **102**, 10451-10453 (2005).

[5] K. S. Novoselov, A. K. Geim, S. V. Morozov, D. Jiang, M. I. Katsnelson, I. V. Grigorieva, S. V. Dubonos, and A. A. Firsov, "Two-dimensional gas of massless Dirac fermions in graphene," *Nature,* **438**, 197-200 (2005).

[6] Y. B. Zhang, Y. W. Tan, H. L. Stormer, and P. Kim, "Experimental observation of the quantum Hall effect and Berry's phase in graphene," *Nature,* **438**, 201-204 (2005).

[7] A. C. Ferrari, J. C. Meyer, V. Scardaci, C. Casiraghi, M. Lazzeri, F. Mauri, S. Piscanec, D. Jiang, K. S. Novoselov, S. Roth, and A. K. Geim, "Raman spectrum of graphene and graphene layers," *Physical Review Letters,* **97**, 187401 (2006).

[8] D. Graf, F. Molitor, K. Ensslin, C. Stampfer, A. Jungen, C. Hierold, and L. Wirtz, "Spatially resolved Raman spectroscopy of single- and few-layer graphene," *Nano Letters,* **7**, 238-242 (2007).

[9] Y. W. Son, M. L. Cohen, and S. G. Louie, "Energy gaps in graphene nanoribbons," *Physical Review Letters,* **97**, 216803 (2006).

[10] M. Y. Han, B. Ozyilmaz, Y. B. Zhang, and P. Kim, "Energy band-gap engineering of graphene nanoribbons," *Physical Review Letters,* **98**, 206805 (2007).

[11] Z. H. Chen, Y. M. Lin, M. J. Rooks, and P. Avouris, "Graphene nano-ribbon electronics," *Physica E: Low-dimensional Systems and Nanostructures,* 228-232 (2007).

[12] J. Bai, X. Duan, and Y. Huang, "Rational fabrication of graphene nanoribbons using a nanowire etch mask," *Nano Letters,* **9**, 2083-2087 (2009).

[13] N. A. Melosh, A. Boukai, F. Diana, B. Gerardot, A. Badolato, P. M. Petroff, and J. R. Heath, "Ultrahigh-density nanowire lattices and circuits," *Science,* **300**, 112-115 (2003).

[14] J. R. Heath, "Superlattice Nanowire Pattern Transfer (SNAP)," *Accounts of Chemical Research,* **41**, 1609-1617 (2008).

[15] J. C. Meyer, A. K. Geim, M. I. Katsnelson, K. S. Novoselov, T. J. Booth, and S. Roth, "The structure of suspended graphene sheets," *Nature,* **446**, 60-63 (2007).

[16] J. Martin, N. Akerman, G. Ulbricht, T. Lohmann, J. H. Smet, K. Von Klitzing, and A. Yacoby, "Observation of electron-hole puddles in graphene using a scanning single-electron transistor," *Nature Physics,* **4**, 144-148 (2008).

[17] M. Ishigami, J. H. Chen, W. G. Cullen, M. S. Fuhrer, and E. D. Williams, "Atomic structure of graphene on SiO_2," *Nano Letters,* **7**, 1643-1648 (2007).

[18] E. Stolyarova, K. T. Rim, S. M. Ryu, J. Maultzsch, P. Kim, L. E. Brus, T. F. Heinz, M. S. Hybertsen, and G. W. Flynn, "High-resolution scanning tunneling microscopy imaging of mesoscopic graphene sheets on an insulating surface," *Proceedings of the National Academy of Sciences of the United States of America,* **104**, 9209-9212 (2007).

[19] E. Stolyarova, D. Stolyarov, L. Liu, K. T. Rim, Y. Zhang, M. Han, M. Hybersten, P. Kim, and G. Flynn, "Scanning tunneling microscope studies of ultrathin graphitic (graphene) films on an insulating substrate under ambient conditions," *Journal of Physical Chemistry C,* **112**, 6681-6688 (2008).

[20] C. L. Kane and E. J. Mele, "Broken symmetries in scanning tunneling images of carbon nanotubes," *Physical Review B,* **59**, R12759-R12762 (1999).

[21] D. C. Elias, R. R. Nair, T. M. G. Mohiuddin, S. V. Morozov, P. Blake, M. P. Halsall, A. C. Ferrari, D. W. Boukhvalov, M. I. Katsnelson, A. K. Geim, and K. S. Novoselov, "Control of graphene's properties by reversible hydrogenation: evidence for graphane," *Science,* **323**, 610-613 (2009).